

Real-time Transmission of Geometrically-shaped Signals using a Software-defined GPU-based Optical Receiver

SJOERD VAN DER HEIDE^{1,*}, RUBEN S. LUIS²,
SEBASTIAAN GOOSSENS¹, BENJAMIN J. PUTTNAM²,
GEORG RADEMACHER², TON KOONEN¹, SATOSHI SHINADA²,
YOSHINARI AWAJI², ALEX ALVARADO¹, HIDEAKI FURUKAWA²,
CHIGO OKONKWO¹

¹*Department of Electrical Engineering, Eindhoven University of Technology, PO Box 513, 5600 MB, Eindhoven, the Netherlands*

²*National Institute of Information and Communications Technology, Photonic Network System Laboratory, 4-2-1, Nukui-Kitamachi, Koganei, Tokyo, 184-8795, Japan*

**s.p.v.d.heide@tue.nl*

Abstract: A software-defined optical receiver is implemented on an off-the-shelf commercial graphics processing unit (GPU). The receiver provides real-time signal processing functionality to process 1 GBaud minimum phase (MP) 4-, 8-, 16-, 32-, 64-, 128-ary quadrature amplitude modulation (QAM) as well as geometrically shaped (GS) 8- and 128-QAM signals using Kramers-Kronig (KK) coherent detection. Experimental validation of this receiver over a 91 km field-deployed optical fiber link between two Tokyo locations is shown with detailed optical signal-to-noise ratio (OSNR) investigations. A net data rate of 5 Gbps using 64-QAM is demonstrated.

© 2022 Optica Publishing Group under the terms of the [Optica Publishing Group Publishing Agreement](#)

1. Introduction

In recent years, graphics processing units (GPUs) have been proposed as an alternative to field-programmable gate arrays (FPGAs) [1]–[3] and application-specific integrated circuits (ASICs) for optical communications [4]–[12]. More than a decade of steady exponential improvement of computation capacity (45% yearly increase [13]) and energy efficiency (25% yearly increase [14]) of GPUs have accelerated its potential applications in the field of optical communications. Recent demonstrations include real-time forward error correction (FEC) decoding [4], [5], physical-layer functionality [6]–[8], differential quaternary phase-shift-keying (DQPSK) detection [9], and flexible multi-modulation format detection using directly detected pulse-amplitude modulated signals, and coherently detected quadrature amplitude modulation (QAM) signals [10]–[12] using Kramers-Kronig (KK) detection [15]. We demonstrated a real-time receiver over a 10,000 km straight-line link [12] and a field-deployed fiber [11].

In this work, the flexible, software-defined real-time multi-modulation format receiver is optimized for improved performance and demonstrated modulation formats are extended with odd-power QAM and geometric shaping (GS). A commercial off-the-shelf GPU is used for real-time digital signal processing of minimum phase (MP) 4-, 8-, 16-, 32-, 64-, and 128-QAM as well as geometrically-shaped 8-QAM and 128-QAM signals using KK coherent detection [15]. The receiver is experimentally validated using a field-deployed transmission link between two Tokyo locations with dynamic components of the receiver digital signal processing (DSP) handling fluctuations of the environmental conditions. Detailed investigations into optical signal-to-noise ratio (OSNR) performance are shown and carrier-to-signal power ratio (CSPR) is optimized for all transmission scenarios. Net throughput is calculated for the evaluated formats

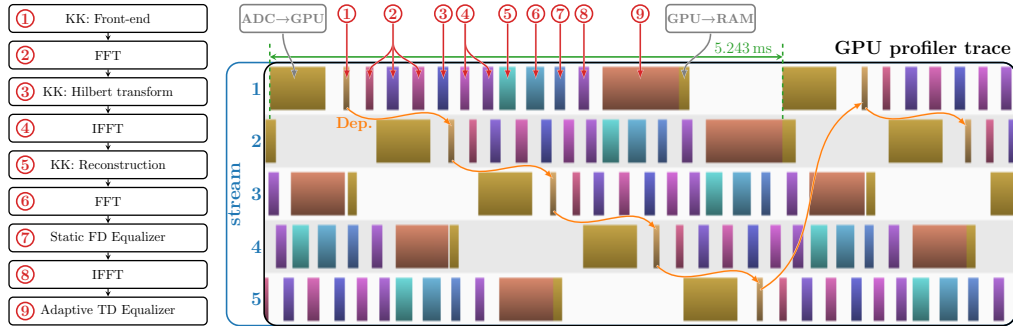


Fig. 1. Real-time Kramers-Kronig digital signal processing chain including GPU profiler trace, additional details in [11].

and multiple hard decision forward error correction (HD-FEC) algorithms, with 64-QAM paired with a 20% overhead HD-FEC achieving a net throughput of 5 Gbps at 28.2 dB OSNR.

This paper is an extension to [11]. The demonstrated capabilities of the real-time receiver are extended to show support for odd-power QAM and geometrically-shaped constellations. Furthermore, the performance of the receiver with respect to [11] is improved through several optimizations; Firstly, the power of the digitally-inserted carrier tone with respect to the signal (CSPR) is optimized. In [11], a static CSPR value was used, here, a detailed investigation into the influence of CSPR on transmission performance is presented. Secondly, the reconfigurable optical add-drop multiplexers (ROADMs) are removed from the transmission path and replaced by an erbium-doped fiber amplifier (EDFA) at the remote site, enabling evaluation of the receiver at higher OSNR. Thirdly, the 1 GHz photodiode is replaced by a 6.5 GHz model, significantly improving the receiver bandwidth. Fourthly, the gap between the signal and digitally-inserted carrier is optimized, resulting in the use of a smaller gap. Fifthly, launch power is optimized, but we observe no significant launch power dependence on OSNR performance. These changes and optimizations substantially improve transmission performance compared to what we presented in [11]. Finally, more modulation formats are evaluated, 4-, 8-, GS-8-, 16-, 32-, 64-, 128-, and GS-128-QAM to comprehensively demonstrate multi-modulation format receiver capability.

2. Digital signal processing chain

Fig. 1 shows the real-time DSP chain for KK coherent N-QAM signals. Here, an overview of its GPU-based implementation is given. A more detailed description can be found in [11]. First, buffers containing 2^{22} digitized samples are transferred from analog-to-digital converter (ADC) to GPU in real time using direct memory access (DMA). The signal processing starts with a GPU kernel converting samples received as 12-bit fixed point to 32-bit floating point numbers, adding the appropriate DC offset, and performing the square root and logarithm KK front-end operations. This first kernel is annotated by the number 1 in Fig. 1. In step 3, enabled by a pair of 100% overlap-save 1024-point fast Fourier transforms (FFTs), the phase of the optical signal is recovered by a frequency-domain Hilbert transform. This phase is combined with the amplitude calculated in step 1 to reconstruct the optical signal [15] which is subsequently downconverted for further processing. Another pair of FFTs supports frequency-domain static equalization and resampling from 4 to 2 samples-per-symbol. Finally, a 4-tap adaptive time-domain widely-linear [16] decision-directed least mean square (DD-LMS) equalizer is employed to recover the signal. The minimum Euclidean distance decisions made by the equalizer are demapped into bits and sent to random-access memory (RAM).

Full utilization of GPU resources is achieved through massive parallelization within kernels

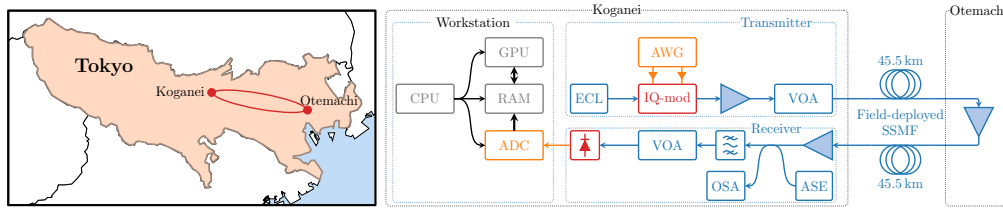


Fig. 2. Experimental setup with a field-deployed link between Koganei and Otemachi, Tokyo, Japan.

as well as operating multiple processing streams in parallel. Most of the kernels operating within each stream are highly parallel themselves, e.g. the FFTs, Hilbert transform, and the frequency-domain equalizer. However, algorithms such as the adaptive time-domain equalizer are hard to parallelize due to its sequential nature and time-dependencies of the tap updates. The use of multiple processing streams allows these hard-to-parallelize algorithms to run next to easy-to-parallelize algorithms. Therefore, even though the adaptive equalization takes up significant amount of *time* as shown in the GPU profiler trace in Fig. 1, significant amount of *resources* is not required. This concept and many other implementation strategies are discussed in detail in [11]. Constellation cardinality only slightly influences GPU resource utilization. The KK algorithm and static equalization take up the majority of computational resources.

Note that several parameters of the real-time receiver are static and optimized offline. Since the ADC is AC-coupled, the DC-term of the signal is lost. This DC-term is crucial for correct signal reconstruction and is added in step 1 as described above. The question remains how to determine the optimal value since it is dependent on the signal power, noise power, and CSPP. Throughout this work, all measurements are performed multiple times using different DC offset values to ensure the optimal performance is observed. Alternatively, one could implement an algorithm to calculate and update the optimal DC-term in real time [17].

Similarly, the 203-tap static frequency-domain equalizer is optimized offline using a training sequence every time that the data acquisition is initialized. Therefore, the entire signal processing chain up to the adaptive equalizer is agnostic to the modulation format. The adaptive equalizer only needs to know the constellation since, after initial setup and convergence using a training sequence, it is updated in a blind decision-directed fashion where part of a buffer is used to update equalizer taps for subsequent buffers. Also, the symbol decisions are demapped into bits and are considered as the output of the DSP chain. The constellation points and bit mapping are uploaded to the GPU for the equalizer to make decisions based on a minimum Euclidean distance criterion. Note that no phase compensation algorithm is required since the KK coherent receiver scheme is free of phase noise. Furthermore, the DSP chain does not rely on specific properties of modulation formats such as symmetry. Therefore, support for various geometrically-shaped constellations is achieved by uploading the location of the constellation points and corresponding bit mapping for the equalizer and demapper to use.

3. Experimental Setup

Fig. 2 shows the experimental setup using the field-deployed link between Koganei and Otemachi, Tokyo. First, an 8-bit 12 GS/s arbitrary-waveform generator (AWG) generates MP 1 GBaud QAM signals with 1% rolloff root-raised-cosine (RRC) pulse shaping with a digitally inserted carrier tone at 0.516 GHz. The 2^{20} N-ary symbol sequence is generated using PCG64 pseudo-random numbers and mapped to the desired modulation format. Both conventional and geometrically shaped QAM formats are employed, the latter optimized for the additive white Gaussian noise (AWGN) channel and generated through an iterative optimization process similar to [18]. Further

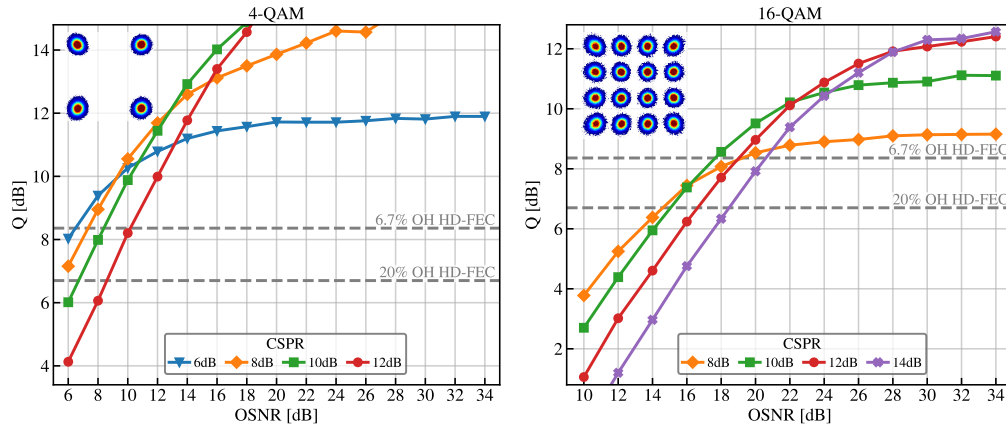


Fig. 3. Q-factor versus OSNR after transmission through 91 km of field-deployed SSMF for 4-QAM and 16-QAM for various CSRs. Insets show constellations with highest Q-factor without noise loading with 12 dB CSR for 4-QAM and 14 dB for 16-QAM.

details can be found in Section 5.

A 16 GHz in-phase and quadrature modulator (IQM) modulates the signal onto a 100 kHz linewidth 1550.51 nm external cavity laser (ECL). The amplified signal is launched into 45.5 km of field-deployed standard single-mode fiber (SSMF) at a fixed launch power. At the other location in Otemachi, Tokyo, an EDFA amplifies the signal again to the same launch power and it is transmitted back to Koganei via 45.5 km of SSMF. 56% of this fiber is installed in underground ducts and the remainder on aerial paths and in the surface along railway tracks.

At the receiver, the signal is amplified, combined with amplified spontaneous emission (ASE) from a noise-loading stage to vary the OSNR, and filtered using a 5 GHz bandpass filter (BPF). A variable optical attenuator (VOA) controls the optical power into the 6.5 GHz photodiode such that the electrical output swing fills the 1 GHz 4 GS/s 12-bit ADC detection range. Receiver clock is synchronized to the transmitter and DSP is performed in real time on the GPU with 5120 processing cores as described in Section 2. Error counting is performed offline over 98 buffers containing 2^{20} symbols each.

Several optimizations have been employed to increase OSNR performance. Firstly, no significant dependence of launch power on OSNR performance was observed. Therefore, the launch power was fixed. Next, the gap between the digitally-inserted carrier required for KK detection was optimized. With the 1% roll-off RRC 1 GBaud signal ending at 0.505 GHz and the carrier tone at 0.516 GHz, a gap of only 11 MHz was left. One would expect a larger gap to be more beneficial since it reduces signal-signal beat interference (SSBI) which when not entirely removed by the KK algorithm leaves reconstruction errors. However, the ADC has a limited 3 dB bandwidth of 1 GHz, thus impairing the signal after detection but crucially before the KK algorithm, leading to imperfect reconstruction. It is expected that the penalty from increased imperfect reconstruction obstructs the use of a larger gap. Finally, the power of the digitally-inserted carrier tone relative to the signal, the CSR, is varied and reported in the next section.

4. Results

Fig. 3 shows the Q-factor versus OSNR for 4-QAM and 16-QAM for multiple CSRs. It is clear that lower CSR values perform better in the low OSNR regime and higher CSRs at higher OSNR. Note that total signal power as defined in the OSNR includes both the carrier tone and the

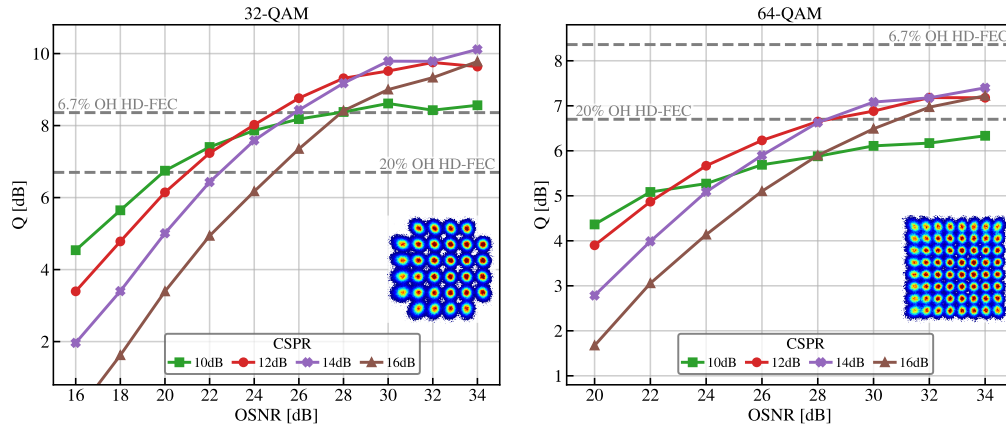


Fig. 4. Q-factor versus OSNR after transmission through 91 km of field-deployed SSMF for 32-QAM and 64-QAM for various CSPRs. Insets show constellations with highest Q-factor without noise loading with 16 dB CSPR.

N-QAM signal. Therefore, if CSPR is increased, signal power decreases, signal-to-noise ratio (SNR) decreases, and Q-factor decreases. This is especially relevant at low OSNRs, because optical noise is dominant in this regime. Conversely, if CSPR is increased, carrier power increases, SSBI decreases, fewer reconstruction errors occur, and Q-factor increases. This is relevant at higher OSNRs, because reconstruction errors are dominant in this regime. Reconstruction errors originate from minimum-phase condition violations and predominantly distort the outer points of a constellation as can be seen in the insets of Fig. 3 [15]. The CSPR trade-off between noise and reconstruction errors is observed for all tested modulations.

4-QAM with 6 dB CSPR reaches the 6.7% overhead HD-FEC Q-factor threshold of 8.35 dB [19] at 6.5 dB OSNR. For this specific CSPR, the Q-factor never exceeds 12 dB whilst higher CSPRs have a lower error floor or Q-factor ceiling. The optimal CSPR depends on the operating regime of the transmission link, the modulation format, and the FEC algorithm employed. Q-values above 15 dB are not displayed in Fig. 3 because too few errors were recorded for statistical significance. 16-QAM reaches the 20% overhead HD-FEC Q-factor threshold of 6.70 dB [20], [21] at 14.6 dB OSNR using a CSPR of 8 dB. The 6.7% overhead HD-FEC is reached at an OSNR of 17.6 dB using 10 dB CSPR.

OSNR performance for 32-QAM and 64-QAM are shown in Fig. 4. 32-QAM is able to reach both the 20% and 6.7% overhead FEC limit at 19.9 dB and 24.9 dB, respectively. However, 64-QAM is not able to reach the 6.7% overhead FEC threshold, but reaches the other threshold at 28.2 dB. The successful transmission of 64-QAM is enabled by improving receiver bandwidth, increasing OSNR, and optimizing CSPR.

Fig. 5 depicts the OSNR performance for both conventional and geometrically-shaped 8-QAM. The GS format outperforms its conventional counterpart and reaches the 6.7% overhead threshold at 12.0 dB versus 13.0 dB for the conventional format. Similarly, at the 20% threshold, GS-8-QAM outperforms 8-QAM by 1.0 dB and reaches the threshold at 9.4 dB compared to 10.4 dB for 8-QAM.

Fig. 6a shows the Q-factor as a function of OSNR for all evaluated modulation formats aggregated in one figure. For each OSNR, the highest measured Q-factor for that modulation format is plotted, effectively tracing a line along the maximum Q-factor of each modulation format in Figs. 3 to 5 and 128- and GS-128-QAM. As a result, CSPR is optimized for each OSNR. Using this optimization approach, 4-, GS-8-, 8-, 16-, and 32-QAM reach the 6.7% HD-FEC threshold. 64-QAM only reaches the 20% HD-FEC threshold, but 128- and GS-128-QAM

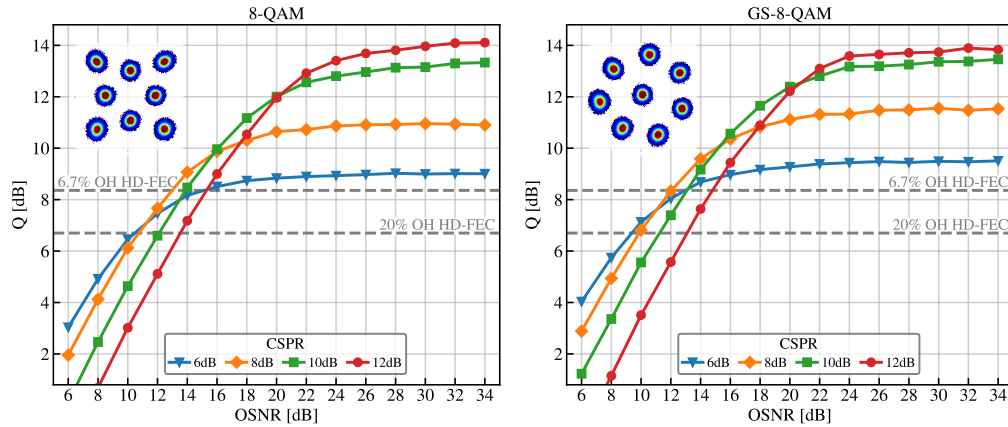
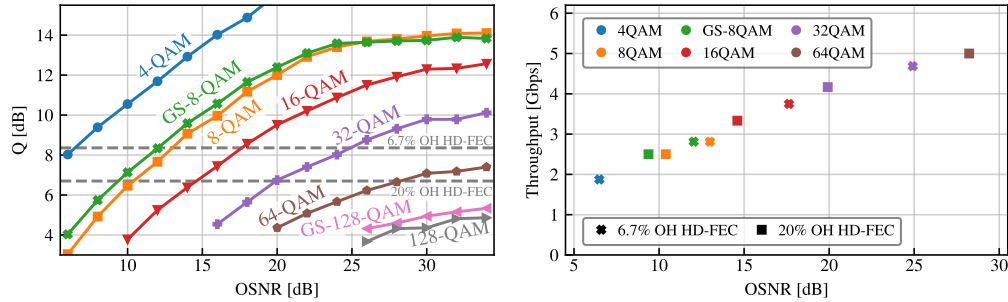


Fig. 5. Q-factor versus OSNR after transmission through 91 km of field-deployed SSMF for 8-QAM and GS-8-QAM for various CSPRs. Insets show constellations with highest Q-factor without noise loading with 12 dB CSPR.



(a) Q-factor versus OSNR for all evaluated modulation formats at optimized CSPR. (b) Net throughput as a function of OSNR for the evaluated modulation formats and HD-FEC thresholds.

Fig. 6. Further analysis of all measurements.

unfortunately stay below the thresholds.

Fig. 6b estimates the net throughput of the transmission system at various OSNRs. For each of the HD-FEC threshold crossings mentioned above, the net data rate after FEC decoding at the OSNR of the crossing is plotted. This figure reveals interesting choices for the system designer. If the system operates above an OSNR of 28.2 dB, 64-QAM combined with a 20% overhead HD-FEC can be employed for a net data rate of 5 Gbps. Alternatively, a lower complexity HD-FEC with an overhead of 6.7% can be paired with 32-QAM for a net data rate of 4.7 Gbps, requiring 24.9 dB OSNR. The multi-modulation format software-defined DSP allows for efficient operation from 6 dB up to 28 dB OSNR, flexibly switching modulation format depending on OSNR.

5. Discussion

Fig. 7 shows the GS formats used in this work compared with their conventional counterparts. Both GS-8-QAM and GS-128-QAM are optimized for the AWGN channel at SNR values of 14 dB and 20 dB, respectively. The optimization uses an iterative approach similar to [18]. The constellations are initialized using the conventional layout and optimized by iterating between adding perturbations in the form of Gaussian noise to a randomly chosen single point and

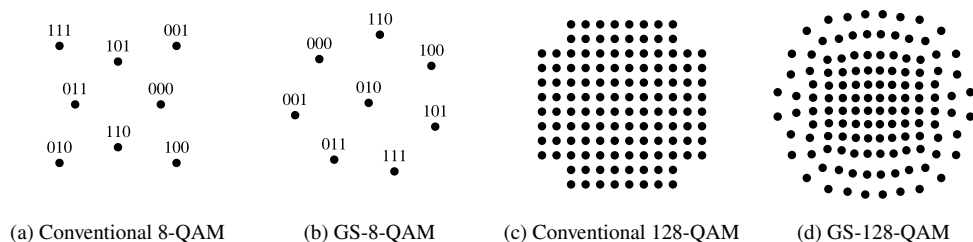


Fig. 7. Comparison between conventional and geometrically-shaped constellations. Drawn using the same scale with normalized power.

swapping the binary labels of two randomly chosen constellation points until convergence is reached. After each iteration, the generalized mutual information (GMI) for the AWGN channel is evaluated and if gains are found, the modified constellation is taken as the new baseline. GS-8-QAM, see Fig. 7b, resembles a circular 8-QAM with center constellation point [22], but is different since it is not symmetric. Symmetries are added to GS-128-QAM to aid convergence of the constellation design. The result of the optimization algorithm is to increase the Euclidean distance between constellation points that differ more than 1 bit.

GS formats for SNRs were created in steps of 1 dB ranging from 5 dB to 14 dB and 17 dB to 23 dB for 8-QAM and 128-QAM, respectively, and were experimentally tested using the field-deployed link since there is no a priori knowledge of the AWGN channel that best resembles the transmission scenario. Many of the GS formats tested on the transmission link perform worse than their conventional counterparts, but GS-8-QAM optimized for 14 dB SNR and GS-128-QAM optimized for 20 dB show significant experimental gains and are included in this work. The constellation design technique optimizes for AWGN, which is a substantially different channel than the one employed in this work. The gain of GS-8-QAM with respect to 8-QAM in the AWGN channel is 0.5 dB at both FEC thresholds. Fig. 8 shows the influence of KK reconstruction errors on OSNR for various CSPRs. The insets shows that the outer points of a constellation are predominantly distorted. The employed GS-8-QAM is more resilient against these distortions than 8-QAM, enabling operation at lower CSPR. Therefore, it is expected that more advanced optimization techniques taking into account the channel including CSPR and KK reconstruction errors will produce better performing modulation formats. However, determining the best GS modulation format for the transmission scenario was not the goal of this investigation. These suboptimal constellations are included as a proof-of-concept for using GS formats in the flexible multi-modulation format receiver, to demonstrate that the receiver supports non-symmetrical modulation formats, and to demonstrate the use of GS-QAM in KK coherent detection.

In [11], we note that the error floor or Q-factor ceiling of high-cardinality formats is most likely due to low-pass filtering at the receiver causing KK reconstruction errors. Here, we use a photodiode with higher bandwidth, enabling successful processing of 64-QAM signals reaching the 20% overhead HD-FEC Q-factor threshold. Further gains could be made by employing a higher bandwidth ADC as well. Note that the KK reconstruction errors are caused by filtering effects between direct detection at the photodiode and conversion in the ADC [23]. Alternatively, one could implement a second static equalizer before the KK algorithm to counter these filtering effects [24]. The current implementation almost fully utilizes the GPU processing capabilities, but further optimization of the implementation can free up resources for such an additional filtering step.

The main factor limiting baud and data rates in this work is the ADC. The off-the-shelf commercial 12-bit 4 GS/s ADC has a 3 dB bandwidth of 1 GHz, limiting the baud rate to 1 GBaud. The ADC uses an eight-lane PCIe Gen 3 interface to communicate with the GPU,

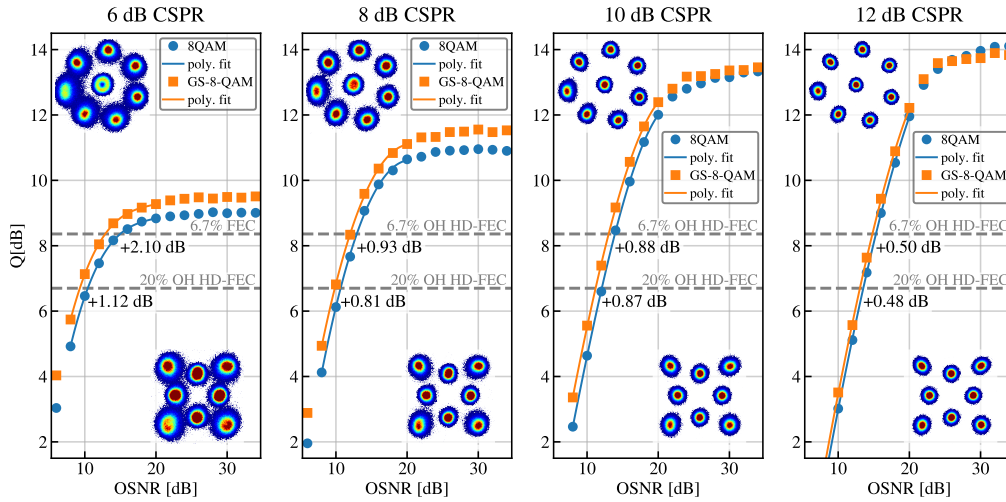


Fig. 8. Q-factor versus OSNR after transmission through 91 km of field-deployed SSMF for 8-QAM and GS-8-QAM for various CSRs. Values indicate OSNR gain of GS-8-QAM with respect to 8-QAM at the specified FEC threshold calculated using a polynomial fit. Insets show constellations with highest Q-factor at 34 dB OSNR.

which limits the sampling rate of the ADC. Future ADCs, employing PCIe Gen 4 or additional lanes, are expected to offer greater sampling rates and bandwidth. Proprietary interfaces such as NVIDIA NVLink (at the time of writing is not available in off-the-shelf ADCs) can support an order of magnitude higher throughput from ADC to GPU and may enable greater increases in sampling rates.

6. Conclusion

A commercial off-the-shelf GPU is used for real-time digital signal processing of minimum-phase 4-, 8-, 16-, 32-, 64-, and 128-QAM as well as geometrically-shaped 8-QAM and 128-QAM signals detected with a KK coherent receiver [15]. This real-time, flexible, multi-modulation format receiver is experimentally validated using a field-deployed link between two Tokyo locations. A net data rate of 5 Gbps is demonstrated using 1 GBaud 64-QAM. This shows the potential of GPUs for software-defined signal processing functionality in optical communication systems.

Funding. This work was partly supported by the Dutch NWO Gravitation Program on Research Center for Integrated Nanophotonics under Grant GA 024.002.033. The work of A. Alvarado and S. Goossens has received funding from the European Research Council (ERC) under the European Union’s Horizon 2020 research and innovation programme (grant agreement No. 757791).

Data availability. Data underlying the results presented in this paper are not publicly available at this time but may be obtained from the authors upon reasonable request.

Disclosures. The authors declare no conflicts of interest

References

- [1] S. Beppu, K. Igarashi, H. Mukai, M. Kikuta, M. Shigihara, D. Soma, T. Tsuritani, and I. Morita, “Real-time strongly-coupled 4-core fiber transmission,” in *Optical Fiber Communication Conference (OFC) 2020*, Optical Society of America, 2020, Th3H.2. doi: 10.1364/OFC.2020.Th3H.2.

- [2] S. Beppu, K. Igarashi, M. Kikuta, D. Soma, T. Nagai, Y. Saito, H. Takahashi, T. Tsuritani, I. Morita, and M. Suzuki, "Weakly coupled 10-mode-division multiplexed transmission over 48-km few-mode fibers with real-time coherent MIMO receivers," *Opt. Express*, vol. 28, no. 13, pp. 19 655–19 668, Jun. 2020. doi: [10.1364/OE.395415](https://doi.org/10.1364/OE.395415).
- [3] S. Randel, S. Corteselli, D. Badini, D. Pilori, S. Caelles, S. Chandrasekhar, J. Gripp, H. Chen, N. K. Fontaine, R. Ryf, and P. J. Winzer, "First real-time coherent MIMO-DSP for six coupled mode transmission," in *2015 IEEE Photonics Conference (IPC)*, 2015. doi: [10.1109/IPCon.2015.7323761](https://doi.org/10.1109/IPCon.2015.7323761).
- [4] R. Li, J. Zhou, Y. Dou, S. Guo, D. Zou, and S. Wang, "A multi-standard efficient column-layered LDPC decoder for Software Defined Radio on GPUs," in *2013 IEEE 14th Workshop on Signal Processing Advances in Wireless Communications (SPAWC)*, 2013, pp. 724–728. doi: [10.1109/SPAWC.2013.6612145](https://doi.org/10.1109/SPAWC.2013.6612145).
- [5] T. Suzuki, S. Kim, J. Kani, T. Hanawa, K. Suzuki, and A. Otaka, "Demonstration of 10-Gbps Real-Time Reed–Solomon Decoding Using GPU Direct Transfer and Kernel Scheduling for Flexible Access Systems," *Journal of Lightwave Technology*, vol. 36, no. 10, pp. 1875–1881, 2018. doi: [10.1109/JLT.2018.2793938](https://doi.org/10.1109/JLT.2018.2793938).
- [6] T. Suzuki, S. Kim, J. Kani, A. Otaka, and T. Hanawa, "10-Gb/s Software Implementation of Burst-Frame Synchronization Using Array-Access Bitshift and Dual-Stage Detection for Flexible Access Systems," *Journal of Lightwave Technology*, vol. 36, no. 23, pp. 5656–5662, 2018. doi: [10.1109/JLT.2018.2870912](https://doi.org/10.1109/JLT.2018.2870912).
- [7] T. Suzuki, S. Y. Kim, J. I. Kani, and J. Terada, "Software Implementation of 10G-EPON Upstream Physical-Layer Processing for Flexible Access Systems," *J. of Lightw. Technol.*, vol. 37, no. 6, pp. 1631–1637, Mar. 2019. doi: [10.1109/ACCESS.2019.2904083](https://doi.org/10.1109/ACCESS.2019.2904083).
- [8] T. Suzuki, S. Kim, J. Kani, and J. Terada, "Demonstration of Fully Softwarized 10G-EPON PHY Processing on a General-Purpose Server for Flexible Access Systems," *Journal of Lightwave Technology*, vol. 38, no. 4, pp. 777–783, 2020. doi: [10.1109/JLT.2019.2948333](https://doi.org/10.1109/JLT.2019.2948333).
- [9] T. Suzuki, S. Kim, J. Kani, and J. Terada, "Real-Time Implementation of Coherent Receiver DSP Adopting Stream Split Assignment on GPU for Flexible Optical Access Systems," *J. of Lightw. Technol.*, vol. 38, no. 3, pp. 668–675, Feb. 2020. doi: [10.1109/JLT.2019.2950155](https://doi.org/10.1109/JLT.2019.2950155).
- [10] S. P. van der Heide, R. S. Luis, B. J. Puttnam, G. Rademacher, T. Koonen, S. Shinada, Y. Awaji, C. Okonkwo, and H. Furukawa, "Real-time, Software-Defined, GPU-Based Receiver Field Trial," *ECOC We1E5*, 2020. doi: [10.1109/ECOC48923.2020.9333244](https://doi.org/10.1109/ECOC48923.2020.9333244).
- [11] S. P. van der Heide, R. S. Luis, B. J. Puttnam, G. Rademacher, T. Koonen, S. Shinada, Y. Awaji, H. Furukawa, and C. Okonkwo, "Field Trial of a Flexible Real-Time Software-Defined GPU-Based Optical Receiver," *J. Lightwave Technol.*, vol. 39, no. 8, pp. 2358–2367, Apr. 2021. doi: [10.1109/JLT.2021.3050304](https://doi.org/10.1109/JLT.2021.3050304).
- [12] S. P. van der Heide, R. S. Luis, B. J. Puttnam, G. Rademacher, T. Koonen, S. Shinada, Y. Awaji, H. Furukawa, and C. Okonkwo, "10,000 km Straight-line Transmission using a Real-time Software-defined GPU-Based Receiver," in *2021 Optical Fiber Communications Conference and Exhibition (OFC)*, 2021, pp. 1–3. doi: [10.1364/OFC.2021.W1I.3](https://doi.org/10.1364/OFC.2021.W1I.3).
- [13] P. J. Winzer and D. T. Neilson, "From Scaling Disparities to Integrated Parallelism: A Decathlon for a Decade," *J. of Lightw. Technol.*, vol. 35, no. 5, pp. 1099–1115, Mar. 2017. doi: [10.1109/JLT.2017.2662082](https://doi.org/10.1109/JLT.2017.2662082).
- [14] Y. Sun, N. B. Agostini, S. Dong, and D. Kaeli, "Summarizing CPU and GPU Design Trends with Product Data," *arXiv:1911.11313 [cs]*, Nov. 2019.
- [15] A. Mecozzi, C. Antonelli, and M. Shtaif, "Kramers Kronig coherent receiver," *Optica*, vol. 3, no. 11, p. 1220, Nov. 2016. doi: [10.1364/OPTICA.3.001220](https://doi.org/10.1364/OPTICA.3.001220).
- [16] E. P. da Silva and D. Zibar, "Widely Linear Equalization for IQ Imbalance and Skew Compensation in Optical Coherent Receivers," *Journal of Lightwave Technology*, vol. 34, no. 15, pp. 3577–3586, 2016. doi: [10.1109/JLT.2016.2577716](https://doi.org/10.1109/JLT.2016.2577716).
- [17] R. S. Luís, G. Rademacher, B. J. Puttnam, C. Antonelli, S. Shinada, and H. Furukawa, "Simple method for optimizing the DC bias of Kramers-Kronig receivers based on AC-coupled photodetectors," *Opt. Express*, vol. 28, no. 3, pp. 4067–4075, Feb. 2020. doi: [10.1364/OE.3833369](https://doi.org/10.1364/OE.3833369).
- [18] B. Chen, C. Okonkwo, D. Lavery, and A. Alvarado, "Geometrically-shaped 64-point constellations via achievable information rates," in *2018 20th International Conference on Transparent Optical Networks (ICTON)*, 2018, pp. 1–4. doi: [10.1109/ICTON.2018.8473932](https://doi.org/10.1109/ICTON.2018.8473932).
- [19] Y. Miyata, K. Kubo, K. Onohara, W. Matsumoto, H. Yoshida, and T. Mizuochi, "UEP-BCH product code based hard-decision FEC for 100 Gb/s optical transport networks," in *OFC/NFOEC*, 2012, pp. 1–3. doi: [10.1364/NFOEC.2012.JW2A.7](https://doi.org/10.1364/NFOEC.2012.JW2A.7).
- [20] M. Scholten, T. Coe, J. Dillard, and F. Chang, "Enhanced FEC for 40G/100G," in *2009 European Conference on Optical Communication (ECOC)*, 2009, pp. 1–12.
- [21] A. i Amat and L. Schmalen, "Forward Error Correction for Optical Transponders," in *Springer Handbook of Optical Networks*. Cham: Springer International Publishing, 2020, ch. 7, pp. 177–257, Table 7.5, isbn: 978-3-030-16250-4. doi: [10.1007/978-3-030-16250-4_7](https://doi.org/10.1007/978-3-030-16250-4_7).

- [22] M. Nölle, F. Frey, R. Elschner, C. Schmidt-Langhorst, A. Napoli, and C. Schubert, "Performance Comparison of Different 8QAM Constellations for the Use in Flexible Optical Networks," in *Optical Fiber Communication Conference*, Optical Society of America, 2014, W3B.2. doi: [10.1364/OFC.2014.W3B.2](https://doi.org/10.1364/OFC.2014.W3B.2).
- [23] X. Chen, C. Antonelli, S. Chandrasekhar, G. Raybon, A. Mecozzi, M. Shtaif, and P. Winzer, "Kramers–kronig receivers for 100-km datacenter interconnects," *Journal of Lightwave Technology*, vol. 36, no. 1, pp. 79–89, 2018. doi: [10.1109/JLT.2018.2793460](https://doi.org/10.1109/JLT.2018.2793460).
- [24] X. Chen, S. Chandrasekhar, S. Olsson, A. Adamiecki, and P. Winzer, "Impact of O/E Front-End Frequency Response on Kramers-Kronig Receivers and its Compensation," in *2018 European Conference on Optical Communication (ECOC)*, 2018, pp. 1–3. doi: [10.1109/ECOC.2018.8535239](https://doi.org/10.1109/ECOC.2018.8535239).